Volume 1 | Number 1 | Jan 2013 | Pages 1–100

PCCP

Physical Chemistry Chemical Physics
www.rsc.org/pccp

ROYAL SOCIETY OF CHEMISTRY

ROYAL SOCIETY OF CHEMISTRY

www.rsc.org/pccp

Si Photoanode Protected by Metal Modified ITO with Ultrathin NiO$_x$ for Solar Water Oxidation

Ke Sun[*a§], Shaohua Shen[b], Justin S. Cheung[a], Xiaolu Pang[c], Namseok Park[a], Jigang Zhou[d], Yongfeng Hu[d], Zhelin Sun[a], Sun Young Noh[e], Conor T. Riley[f], Paul K. L. Yu[a], Sungho Jin[e], Deli Wang[*aeg]

[a]Department of Electrical and Computer Engineering, University of California, San Diego, 9500 Gilman Dr., La Jolla, California 92093, U.S.A

[b]International Research Center for Renewable Energy, State Key Lab of Multiphase Flow in Power Engineering, Xi'an Jiaotong University, Xi'an, Shaanxi 710049, China

[c]Department of Materials Physics and Chemistry, University of Science and Technology Beijing, Beijing 100083, China

[d]Canadian Light Source Inc., Saskatoon, Saskatchewan S7N0X4, Canada

[e]Materials Science and Engineering, Department of Mechanical and Aerospace Engineering, University of California, San Diego, 9500 Gilman Dr., La Jolla, California 92093, U.S.A

[f]Department of NanoEngineering, University of California, San Diego, 9500 Gilman Dr., La Jolla, California 92093, U.S.A

1

[g]Qualcomm Institute, University of California, San Diego, 9500 Gilman Dr., La Jolla, California

92093, U.S.A

[§]current address: Joint Center for Artificial Photosynthesis, Division of Chemistry and Chemical

Engineering, California Institute of Technology, Jorgensen Laboratory, Mail Code 132-80, 1200

East California Blvd, Pasadena, California 91125, U.S.A

Corresponding author

Prof. Deli Wang and Dr. Ke Sun

Emails: deliwang@ucsd.edu, k3sun@ucsd.edu

Telephone: +1.858.822.4723

Fax: +1.858.534.0556

Abstract:

We report an ultrathin NiO_x catalyzed Si np^+ junction photoanode for a stable and efficient

solar driven oxygen evolution reaction (OER) in water. A stable semi-transparent ITO/Au/ITO

hole conducting oxide layer, sandwiched between the OER catalyst and the Si photoanode, is

used to protect the Si from corrosion in an alkaline working environment, enhance the hole

transportation, and provide a pre-activation contact to the NiO_x catalyst. This NiO_x catalyzed Si

photoanode generates a photocurrent of 1.98 mA/cm^2 at the equilibrium water oxidation

potential (E_{OER} = 0.415 V *vs.* NHE in 1 M NaOH solution). A thermodynamic solar-to-oxygen

conversion efficiency (SOCE) of 0.07% under 0.51-sun illumination is observed. The successful

development of a low cost, highly efficient, and stable photoelectrochemical electrode based on

earth abundant elements is essential for the realization of a large-scale practical solar fuel

conversion.

Broader Context:

Reducing the cost and improving the efficiency for solar fuel conversion are essential for practical and scaling-up solar fuel cell applications. Silicon has been proven to be low-cost and scalable to the global scale, however, it is not electrochemically stable when interfacing with aqueous electrolytes when energetic holes are present. On the other hand, it is desirable to replace the noble metal with earth abundant transition metals (Mn, Fe, Co and Ni) for electrocatalysts, which have been demonstrated a high activity in alkaline conditions. Here, we report a stable and efficient Si photoanode with a buried junction protected by a hole conducting ITO using an intermediate metal and eventually catalyzed by an ultrathin NiO_x catalyst.

TCO:
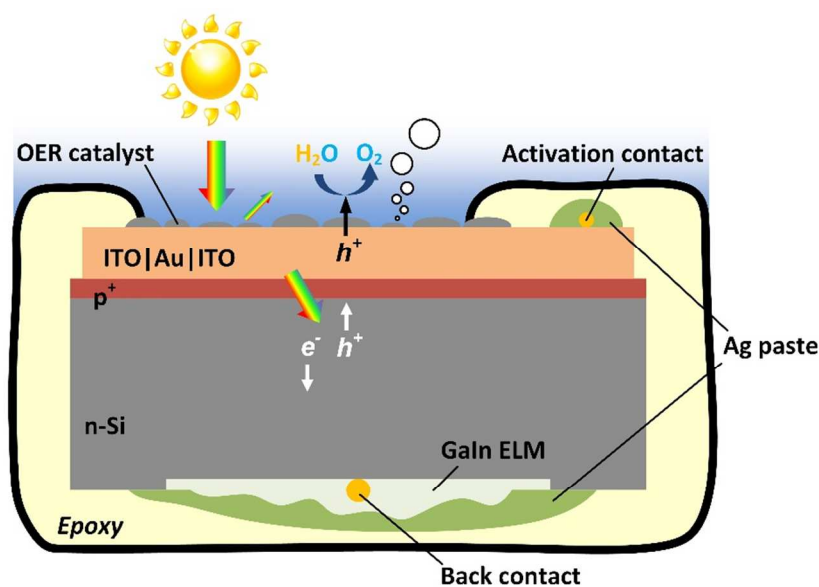
Introduction:

Photoelectrochemical (PEC) solar fuel conversion is one of the very promising approaches to solve energy problems[1]. PEC relies on a separate production process of the electricity generation (free energetic carriers) and the chemical products generation (fuels)[2]. The produced fuels then can be separated, stored, transported, and consumed remotely. Water oxidation for oxygen evolution reaction (OER) in a PEC device is challenging due to the instability of large variety of photo-absorbers under oxidizing conditions (anodic bias or basic electrolyte) by either corrosion or forming an insulating oxide which causes deactivation over time or effectively blocks the photogenerated carriers from reaching the surface for desired water oxidation reaction, respectively. Therefore, realistic photoanodes using materials that are thermodynamically instable need to be properly protected[3]. Therefore, producing a robust and compact interfacial film that protects photoanode materials, provides minimum attenuation to the light absorption as a window layer, also separates and conducts photogenerated hole carriers to the surface, and catalyzes the water oxidation reaction is the key to enabling traditional materials or new material systems for practical solar fuel production[4].

Method using a compact heterogeneous compound coating to isolate the troublesome interface between the photoanode, such as Si, and the oxidizing electrolyte has been developed before. In this method, two interfaces to separate the process of the carrier generation at one (photoelectrical junction) and the process of the chemical fuel formation at the other (electrochemical junction) are utilized to replace the single photoelectrochemical interface formed directly by the photoanode and electrolyte. Materials include metals or metallic silicides[5], wide band gap semiconductors (such as TiO_2[6-9], ZnO[10], WO_3[11], GaN[12], and Fe_2O_3[13]), transparent conducting oxides (TCO, such as mixture of SnO_2 and In_2O_3[14, 15], SnO_2[16, 17] and $Sb/Ru-SnO_2$[18,

[19]), transition metal and its oxides (Ni[20], Fe_2O_3[21], NiO[22, 23], MnO_x[24], and CoO_x[25, 26]), and organic polymers (PEDOT:PSS[27], Polyaniline[28], Polyacetylene[29], and Polypyrrole[30]). Performances of the so-far developed materials or systems greatly depends on the properties of the coating and the two interfaces, such as the barrier height for charge separation, light absorption, photostability/electrochemical stability, hole conductivity, and OER catalytic activity. Noteworthy successes have been achieved in terms of efficiency and stability. For example, Chen et al. used a high quality ultrathin TiO_2 within the tunneling range to protect n-Si photoanode and a thin Ir film for catalyzing OER reaction[8, 31]. This structure showed the champion solar-to-oxygen conversion efficiency (SOCE) of 0.37%, due to the high barrier height defined by the metal-insulator-semiconductor (MIS) junction and the high activity of Ir noble metal. This technique remains challenge both technically on other crystal structures or high profile photo-absorbers and economically due to the use of noble metals. Earth abundant materials are preferred for large-scale production of solar fuels[32]. A few other recent works have demonstrated the capability to use transition metal oxides or single layer of graphene[24, 33] to protect and catalyze n-Si photoanodes for water oxidation. Detailed examinations revealed that the band bending of Si was defined by the metal oxide and the electrolyte semiconductor junctions through the pin-holes or by the equilibrium formed between solution and the metal oxide[21]. Challenges using this approach remains. Specifically, the uniform coating of metal oxide does not provide large surface area which is important for non-noble metal catalysts with inferior catalytic activity. Due to the pin-holes developed during fabrication or operation, the long-term stability of the thin oxide is also a concern[23]. Recently, Dai's group demonstrated a Ni metal directly coated n-Si photoanode with a native oxide showed nearly 100 hours stability in water oxidation condition after Li treatment[20]. This structure shared a few common features as the

device presented in ref [8], where an ultrathin Ni metal (2 nm) served as a metal Schottky contact

for charge separation, a window layer, and a OER catalyst for the Si photoanode. This structure

showed a SOCE of 0.14% under 2-sun illumination. Using TCOs for n-Si photoanode with a

buried junction has been demonstrated before[25, 26, 34]. However, a traditional n-type TCO like

FTO or ITO has a large hole effective mass and a low hole conductivity. On the other hand,

using high work function metal contact would cause significant light attenuation from the thick

protection coatings which lead to decoupling of light absorption and electrochemical reaction[26].

Therefore, the goal of this research is to investigate strategies that can efficiently alter the

photoanode surface using inexpensive and robust methods, and to explore the potential problems

associated with the proposed structure during integration. Specifically, we have synthesized and

characterized an efficient ultrathin porous NiO_x OER nanocatalyst from a low-temperature

hydrolysis method. The effects of the surfactant in the precursor and thermal treatment on its

OER catalytic activity have been systematically investigated. A high work function metal has

been intentionally sandwiched into the traditional n-type ITO to increase its work function,

facilitate the minority hole conduction, and improve the ITO stability. The low-temperature

synthesis, nondestructive electrochemical activation, and low absorption of the catalyst allows

the integration to the protected Si buried junction photoanode. Finally, comparative

performances to the state-of-the art have been summarized.

Experimental:

Ultrathin NiO_x **OER catalyst preparation.** All chemicals were used as it is without further

purification. Aqueous chemical precursors were prepared by mixing nickel acetate ($Ni(Ac)_2$) (50

mM) in ethanol with a non-ionic surfactant Triton-X 100 (with average molar weight of 624.82)

(TX, 0.6 mM) followed by a thorough stirring of the mixture to obtain a clear solution[35]. The deposition of NiO_x on different substrates (Ti foil, FTO glass, n-Si, and np$^+$-junction Si) was carried out by dropping 100-µL precursor, spin-casting at 5000 rpm for 90 s, and heating on a hotplate at 300 ℃ in atmosphere for various time from 10 s to 5 min to remove excessive solvent. The NiO_x OER catalyst (labeled as NiO_x-TX) was synthesized by spin-coating the precursor solution on substrate followed by a thermal annealing as recently reported[35]. For comparison, a catalyst from a similar precursor but without the surfactant (labeled as NiO_x) and a precursor with only the TX surfactant in ethanol (labeled as TX) were also prepared and investigated.

Device fabrication. All the Si substrates were diced into 0.5×0.5 inch^2 and cleaned using diluted HNO_3, acetone, and isopropyl alcohol (IPA) with intermediate DI water rinsing and ultrasonication. Si substrates used in the study included boron doped p$^+$-Si with a bulk resistivity of 0.05 Ω•cm and phosphors doped n-Si with a bulk resistivity of 0.3-0.5 Ω•cm (UniversityWafers). Indium tin oxide and gold (Kurt J. Lesker) sandwich (ITO|Au|ITO) structure (100 nm/5 nm/100 nm) was deposited using the RF magnetron sputtering (Denton) with Ar gas. During the deposition, the pressure in the chamber was kept constant at 10 mTorr. This contact was then thermally annealed at 300 ℃ for 30 s to improve the transmittance and conductivity. To realize an np$^+$-Si junction, we started with an n-Si wafer and diffusion process was performed using a boron-containing spin-on dopant (SOD, Filmtronics, Inc.). 400-µL SOD solution was first spin-coated on a 2″ Si dummy wafer at 3000 rpm for 15 s. The SOD coated dummy wafer together with the samples was immediately transferred to a rapid thermal annealing (RTA) furnace (AG associates Heat Pulse 610). The SOD coated dummy wafer and samples were facing each other separated by quartz spacers with a thickness of 1 mm. The diffusion was then

conducted at 950 ℃ for 120 s under a constant flow of N_2 at 0.85 L/min. After the diffusion process, samples were unloaded from the furnace and immersed in buffered HF etchant (BOE) to remove oxides and residuals. Finally, the back side of diffused samples was then etched using a reactive ion plasma etching (RIE, Oxford P100) with a mixed SF_6/CH_8 (25 sccm/50 sccm) gas at a rate of 3.3 nm/s for 10 min while the front side was protected using a photoresist (PR1818). During etching, the chamber pressure was kept at 15 mTor, the RIE and ICP power were kept at 30 W and 1200 W during the etching process. GaIn eutectic liquid metal (ELM) back contact was then scratched into the Si sample for an ohmic contact to n-Si. Metal wires using were attached to the backside of the Si (photoelectrode contact) and the ITO (activation/solar cell anode contact) using Ag paste (Tedpella 16040-30). Samples made on Ti foil were fixed on a homemade sample holder with the front side area of exact 1 cm by 1 cm exposed to the electrolyte. Samples on FTO glass were fabricated by attaching a Cu wire to the sample surface using the Ag paste. Samples were then embedded in Epoxy (Hysol C1) with only the part covered by NiO_x exposed to the electrolyte. The Cu wire was enclosed in a high-grade polystyrene pipette tip instead of a glass tube to avoid etching in basic solution and introduction of additional contamination to the measurement. Epoxy was dried for overnight before measurement. Sample areas were then measured through the digital images using Photoshop before further measurement.

Solar cell and photoelectrode characterization. Current-voltage (I-V) characteristics of the Si solar cells with ITO|Au|ITO semitransparent contact (s-TCO) and buried junction photoelectrodes with NiO_x OER catalysts were measured using a two-channel potentiostat (Digi-Ivy DY2300). AM 1.5 illumination was achieved with a 150-W xenon-lamp-based solar simulator (Newport Corporation) with an AM 1.5 filter. The light intensity on the masked light

beam was calibrated using a Si photodiode. Effects from the measurement reactor, IR filter, and electrolyte on the light intensity was also measured (Figure s1).

Electrochemical study was conducted using DY2100B potentiostat from Digi-Ivy in a three-electrode configuration. All the measurements were conducted in 1 M NaOH solution (with 17.6 Mohm-cm deionized water) at room temperature in a Taflon container to avoid excessive ions introduced from the glassware etching in this extreme alkaline environment. A Hg/HgO with 1 M NaOH electrode (CH Instruments, CHI 152) and a Pt coil were used as a reference electrode (RE) and a counter electrode (CE), respectively. The reference electrode was placed very close to the working electrode (WE) surface to minimize any uncompensated solution resistance loss and the distance between RE and WE was fixed between measurements. Current density and Tafel slope reported here are without iR correction on the uncompensated resistance loss between the RE and WE. The equilibrium oxygen electrode potential is E^0=0.415 V *vs*. NHE at this condition. The oxygen evolution overpotential is calculated $E-E^0$. Electrolyte was mechanically agitated and purged with N_2 gas before and during measurement. Data collection was conducted using DY2100B software from Digi-Ivy. All the reported potentials are converted to the normal hydrogen electrode (NHE) unless specified.

Surface characterization. The X-ray photoelectron spectroscopy (XPS) measurements were conducted on a Kratos spectrometer (AXIS Ultra DLD) with a monochromatic Al Kα radiation (hν=1486.69 eV) and a concentric hemispherical analyzer. Atomic force microscopic measurement was conducted using a tapping mode atomic force microscope (AFM, Veeco scanning probe microscope) equipped with standard silicon probe (Umasch NSC15/no Al) to evaluate the surface nanoscale topological difference between the thin film coatings. Raw data collected by AFM were processed using NanoScope Software; surface roughness and grain size

were obtained using NanoScope Analysis software. While electrochemical studies of the NiO_x were conducted on samples deposited on fluorine-doped tin oxide glasses (MTI, TEC 15), as well as Ti foils and Si photoanode, the surface morphological study was carried out by AFM (atomic force microscopy) on catalysts coated atomically flat Si (100) substrates and the surface chemical compositional study was performed by XPS (x-ray photoelectron spectroscopy) were conducted on catalysts coated Au coated Ti foils (Alfa Aesar, 10385).

The X-ray Absorption Near Edge Spectroscopy (XANES) were obtained on the spherical grating monochromator (SGM) beamline ($\Delta E/E$: ~10^{-4}) at the Canadian Light Source (CLS) in a surface sensitive, total electron yield (TEY) mode using the specimen current. Data were normalized to the incident photon flux, which were collected with a refreshed gold mesh (evaporation of a fresh Au layer prior to the measurements).

Extracting data from reported I-V curves: The curves were extracted from the corresponding published articles for comparative analysis using the MATLAB Grabit function developed by Jiro Doke download from http://www.mathworks.us.

Results and discussions:

Catalyst activation, OER activity, and stability:

The NiO_x OER catalysts with or without a non-ionic surfactant triton X-100 (labeled as NiO_x-TX or NiO_x, respectively in later discussions) and a control sample with only surfactant (TX) were activated electrochemically and investigated. Cyclic voltammograms (CV at a scan rate 10 mV/s) for the NiO_x OER catalyst coated on a FTO glass without TX are shown in Figure 1a and corresponding Tafel analyses are shown in Figure 1b, which show clear evidence of the cyclic activation. As-prepared NiO_x (black curve) shows a plateau in the potential window of 0.4 - 0.7

V. Tafel slope in this case is 87 mV/dec at 0.7 mA/cm^2, which results in an overpotential of 380 mV to drive an OER current density of 0.52 mA/cm^2. During the second scan, a significant enhancement in the oxidation peak appeared at 0.58 V, as well as a slightly higher reduction peak at 0.5 V (red curve). The Tafel slope at 1 mA/cm^2 dropped to 57 mV/dec and the current density at the overpotential of 380 mV reached 3.34 mA/cm^2. After 500 cycles of activation at a scan rate of 100 mV/s, the magnitude of the oxidation and reduction peaks was further increased and both peaks became sharper with a noticeable asymmetry, and most importantly, the position of the peaks was shifted to higher potential (around 0.63 V) (magenta curve in Figure 1a, at a scan rate of 10 mV/s). Improvements on both the Tafel slope and the overpotential were also noticed. Continued activation for another 310 cycles did not further improve the catalytic activity at the OER current, but the oxidation peak was slightly shifted to a higher potential. This result suggests that the OER activity is definitely maintained after 810 cycles of scan for over 5 hrs of measurements. Note that the TX sample annealed for 30 second (TX-30s) showed a current density comparable to that of the bare FTO within the potential window, which suggested no catalytic activity from the TX treated FTO glass. Active NiO catalysts during the water oxidation have been reported having different phases including the α-Ni(OH)$_2$/γ-NiOOH (α/γ) and the β-Ni(OH)$_2$/β-NiOOH (β/β) transition, where the α/γ transition is typically located at a lower potential with a typically higher equivalent valence state of Ni (3.5-3.67) due to the intercalated cation and water in the NiO$_2$ sheet. On the other hand, β/β transition is typically located at a higher potential with a lower valence state of Ni (2.7-3)[36]. We believe that the plateau in the CV of the as-prepared NiO$_x$ sample indicates a mixed phase of α/γ and β/β transition, as the direct decomposition of nickel precursor did not yield a phase-pure NiO$_x$. The shoulder in the oxidation peak after the first scan suggests that the mixed phases still exist in the catalyst although the α/γ

transition becomes stronger. Anodic-shifted oxidation peak after cyclic activations suggests a phase transition from the α/γ-dominant to the β/β-dominant. Anodic-shifted redox peaks were noticed on the sample that was re-scanned after being stored under normal lab conditions, which is observed for aged α-Ni(OH)$_2$ due to dehydration to β-Ni(OH)$_2$ in ambient. This aged catalyst can then transform back to the γ-NiOOH due to the overcharging of the β-NiOOH[37].

On the other hand, the second CV scans on a NiO$_x$-TX catalyst annealed for different times are shown in Figure 1c. Interestingly, the oxidation peaks from the NiO$_x$-TX annealed for 30 sec and 1 min were located at potentials around 0.65 V and 0.63 V, respectively (Figure 1c). These were about 70 and 50 mV higher than that for the NiO$_x$ case, respectively. Increasing the annealing time from 30 sec to 1 min reduced the overpotential from 357 to 341 mV and the Tafel slopes at 1 mA/cm^2 current density from 63 to 56 mV/dec (Figure 1d). The calculated exchange current density obtained by fitting the Tafel behavior was 7.8×10^{-7} mA/cm^2 from the NiO$_x$-TX annealed for 1 minute. For catalysts that were annealed for 2 and 5 minutes, no significant reduction/oxidation peaks or improved Tafel behavior were noticed suggesting a diminished organized phase and possibly reduced active sites with the increased annealing time. Moreover, cyclic activation over 1 hr did not show improved OER activity on these two samples with a longer annealing time. The oxidation peaks located at higher potential suggest an inherent β/β phase in NiO$_x$-TX catalysts without a cyclic activation. Presumably, this is because the surfactant has the effect of complexing the metal ions, so that the individual oxides do not form prematurely. Such complexing effect is well known in the powerful sol-gel technique for the nanophase formation. However, this sample after more than 500 cyclic scans showed a formation of the second peak at lower potentials, suggesting an occurrence of the α/γ phase transition (Figure s1). Overheating of the catalyst material suppresses the magnitude of the

oxidation/reduction peaks and more importantly degrades the OER activity[4]. This overheating effect on the NiO$_x$-TX activation was also observed on a gas-phase sputtered nickel oxide film, where the film annealed in an inert gas atmosphere at 400 ºC showed a significant lower OER activity and a less chance to be activated than the as-sputtered ones within a fixed number of activation cycles (data not shown). In summary, a careful control of the catalyst preparation conditions, such as concentration of the complexing agents or altering the sintering process, can result in an active catalyst without going through potentially destructive and energy/time-consuming activation processes. Experiments conducted on Ti foil and Au coated Ti foil also showed similar trends with some variations in the current densities due to the differences in the surface roughness, substrate stability, and series resistance. Direct probing on the active phase of catalysts during reaction is needed to fundamentally understand the activation process, which is currently under investigation through an in-situ study in our group and will be reported elsewhere.
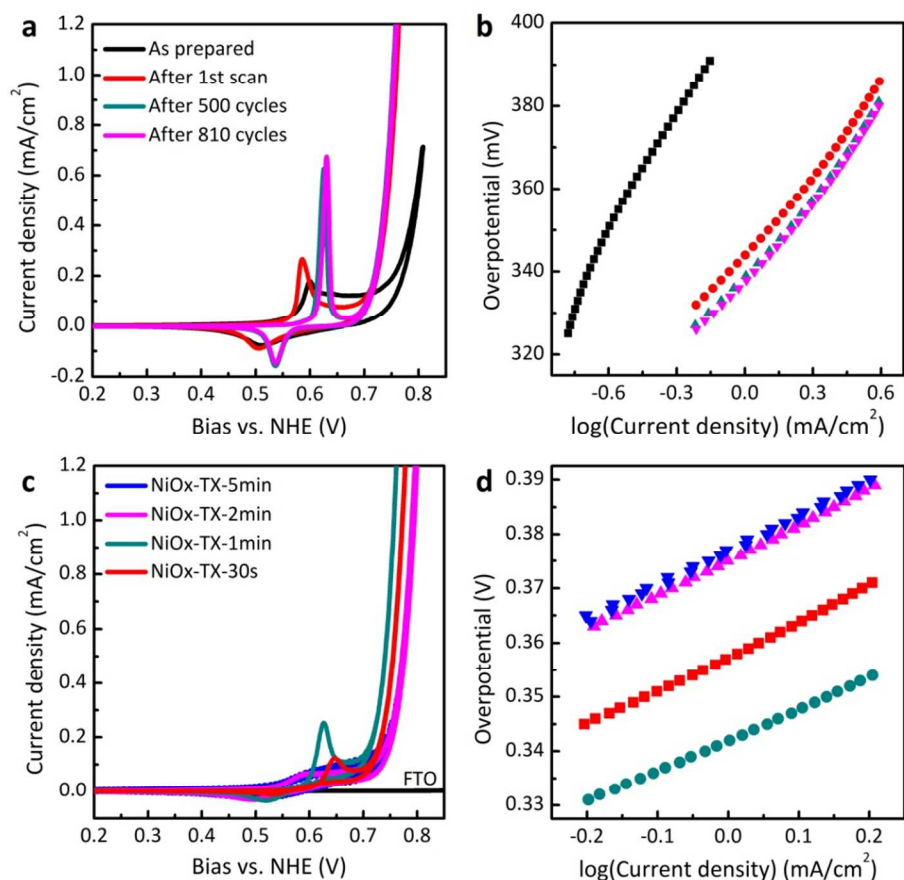
Fig.1 CV curves and Tafel plots of the NiO$_x$ (a and b) annealed for 30 seconds with different activation cycles, and the NiO$_x$-TX (c and d) annealed at 300 ºC for various times.

Ultrathin NiO$_x$ OER catalysts - effects of surfactant and annealing temperature:

The structural formulas of precursors and reaction process are illustrated in Figure 2a. Morphologies of the Si surface coated with and without the complexing agent annealed for 30 seconds at 300 ºC are shown in Figure 2b and 2c. AFM studies revealed a film with dense and compact nanoparticles in NiO$_x$-TX, while NiO$_x$ showed sparse assemblies. The presence of a complexing agent in the precursor affects the physical and morphological properties of the thin film. The TX surfactant possesses a polar head group attached to a long chain aliphatic non-polar

tail. Similar to the observation reported by Canfield et al.[38], the metal-surfactant complexes can be formed. Meanwhile, the long chain Ni-TX complex could also act as a spacer[39]. Thus the presence of a non-ionic surfactant TX, which bears a chain of approximately 10 ether groups, played a crucial role in organizing the structure of the material and in creating well-defined and reproducible nanophases[40]. Sintering the nanoparticles at a high temperature under a higher hydrolysis rate or for a longer period of time was avoided due to the formation of large particles from coalescence of small particles[41]. This may directly affect the catalytic activity due to the reduced active sites, as seen in Figure 1d.
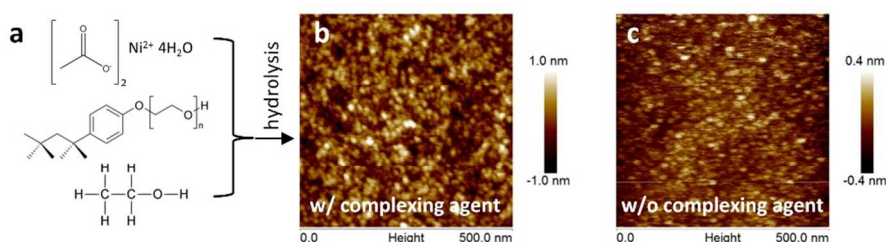
Fig.2 Structural formulas of the precursors (a) and AFM images on the NiO_x catalysts coating on a polished crystal Si with (b) and without (c) the triton-X complexing agent in the precursors.

We used the XPS analysis to study the chemical composition of the catalysts prepared from different precursors and by different annealing times. Ni 2p spectra of a bare Au substrate, TX, NiO_x, and NiO_x-TX annealed for 30 second are shown in Figure 3a. No Ni peak was noticed on the bare substrate or the TX coated substrate. A stronger signal was noticed on NiO_x-TX compared to the NiO_x suggesting a denser film consistent with the AFM observations. O 1s spectrum revealed that the peak at a bare substrate at the binding energy of 532.8 eV was probably from the carbon contamination in the form of C-O (Fig.3b). Appearance of the peak at binding energy of 530.54 eV was presumably due to the formation of Au_2O_3 during the annealing in air. Deconvolution of O 1s peaks of NiO_x and NiO_x-TX using the classical oxygen

fitting revealed existence of oxygen in forms of the lattice oxygen (529.46 eV), hydroxyl group

(531.41 eV) and surface-absorbed water (532.67 eV). The appearance of the new peak at 529.46

eV with the increasing annealing time suggested the increased lattice oxygen and the formation

of NiO_x. The increasing intensity ratio between 529.46 eV and 531.41 eV partially suggested a

decreasing valence state of Ni along with annealing. Interestingly, the high resolution C 1s

spectra revealed not only the presence of the carbon contamination in the form of a C-C group at

the binding energy of 284.8 eV, but also a peak typically recognized from the carboxylate group

at the binding energy around 288 eV potentially from $Ni(Ac)_2$ (Fig.3c)[42]. Note that this peak was

not resolved from samples made from precursors containing only $Ni(Ac)_2$ and certainly not from

TX in ethanol annealed at the same temperature. This was a sign of the Ni-TX complex

formation in the precursor. Higher intensity at the binding energy of 284.8 eV could be a sign of

a higher carbon concentration on the surface due to the C-C or C=C groups from the partially

decomposed Ni-TX complexes. Therefore, annealing for 30 seconds may not lead to a complete

removal of the organic compound[43]. It could also suggest that acetate caped nanoparticles could

be also formed[44]. The physical reasons behind this observation are not absolutely clear at this

point, which needs future study. However, carbon residuals could potentially facilitate the charge

transfer between catalytic active sites and substrate and aid the activation process. Moreover, the

carboxylate component was also present in the sample prepared with a higher concentration of

surfactant (Figure s2). These observations suggested a surfactant effect from the complexing

agent on the decomposition of precursors.

We also used the XPS to examine the effect of the annealing time on the chemical composition

of NiO_x-TX (Figure 3d). High resolution Ni 2p spectra showed a larger peak at a lower energy

with the increased annealing time indicating an improved stoichiometry, which is believed to

have a strong effect on the catalytic activity. In addition, Ni 2p spectra showed an observable

change in the peak shape with the change of the annealing time. This result is consistent with the

O 1s spectrum (Figure 3e) in which an increased intensity of the lattice oxygen at the binding

energy of 529.46 eV was noticed. Although the Ni 2p3/2 peak could originate from different

sources of Ni^{2+} species (partially decomposed nickel acetate-surfactant complexes, $Ni(OH)_2$ and

NiO), one can effectively control the crystallization process and tune the catalytic activity by

controlling the annealing time at a low temperature for the NiO_x catalyst. High resolution C 1s

spectrum (Figure 3f) further showed that the peak at 288 eV reduced its intensity with the

increasing annealing time indicating a further completed decomposition of precursors.

The shape of the Ni L-edge spectra from the XANES measurement showed that the Ni was

mainly in the 2^+ valence state in all the samples, but the existence of Ni^{3+} cannot be excluded,

which is consistent with the XPS results. The shift of the absorption edge to lower energy and the

increase of the peak ratio between ~856.2 eV and ~858.4 eV at the L_3 edge of the samples with

the increased annealing time clearly indicated an improved stoichiometry (Figure s3)[45]. Since Ni

L-edge is a direct probe of Ni 3d vacancy, an increase of Ni 3d vacancy in NiO_x can only be

caused by an enhanced ionic bonding contribution from the Ni-O bond in the samples with a

longer annealing time.
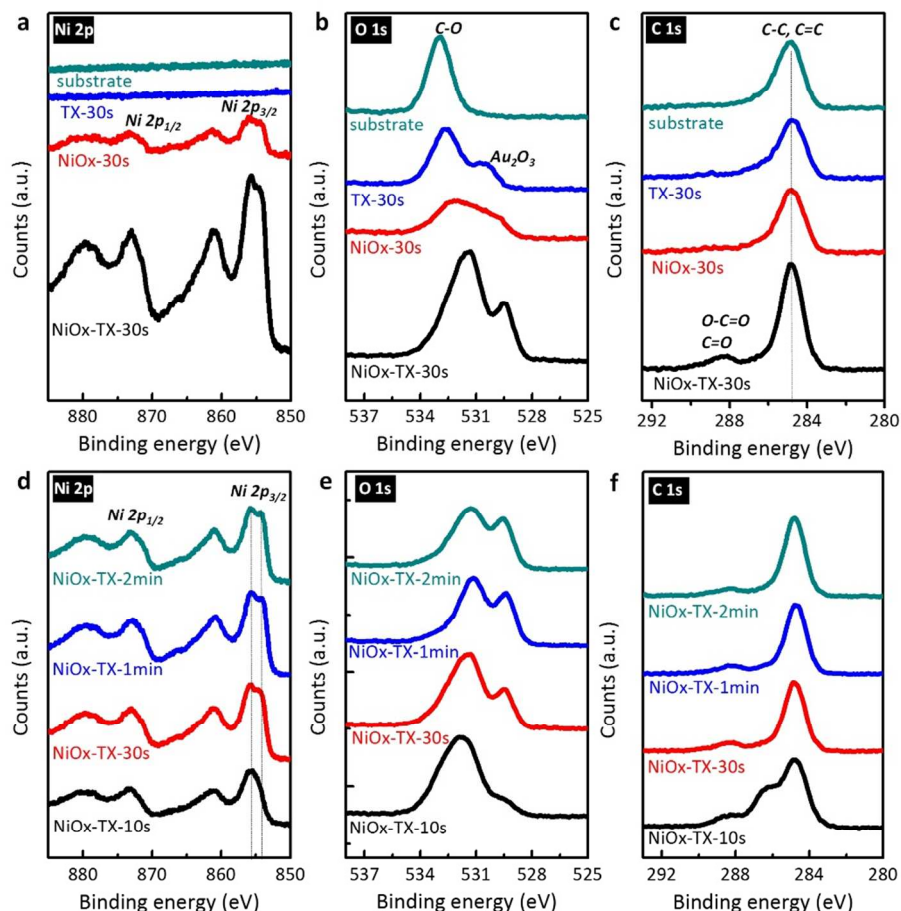
Fig.3 XPS spectra of (a) Ni 2p, (b) O 1s, (c) C 1s on control samples, NiO_x, and NiO_x-TX without complexing agent. XPS spectra of Ni 2p (d), O 1s (e) and C 1s (f) on NiO_x-TX catalysts annealed for various times.

Si photoanode:

The ultrathin NiO_x-TX only is not able to directly protect the Si photoanode due to the porous nature of the nanoparticles, where a continuous drop of photocurrent was noticed (Figure s3). Exposure of Si to an extreme alkaline environment results in an corrosion of Si[46] and eventually causes the loss of catalysts. An interfacial TCO is thus introduced for protection. This interfacial TCO also serves as a component to decouple the photovoltaic cell and the overlaying

18

electrocatalyst, which allows in-situ characterization of the photovoltaic performance and also the pre-activation of the OER electrocatalyst.

Photovoltaic measurement was first conducted *in-situ* in the measurement setup filled with the electrolyte (1 M NaOH) with an IR filter under masked illumination, which resulted nearly half of the intensity loss due to our measurement setup (Figure s4). The current density vs. potential behavior of a representative Si photoanode is shown in Figure 4a. A Schottky junction between ITO|Au|ITO and n-Si was able to provide a small V_{oc} under illumination due to the Fermi level pinning. The Si np^{+} homogeneous junction exhibited a better photovoltaic performance with a larger V_{oc} and J_{sc} due to the improved junction configuration comparing to the one without the inversion layer. Light loss at the NiO_x-TX catalyst is ignorable due to the large band-gap and the small thickness. However, during the active reaction particularly during oxidation, NiO_x could attenuate the light up to 10% in the wavelength range of 400-950 nm due to its electrochromic property[47].

Cyclic activation of the NiO_x-TX catalyst was then conducted prior to the PEC measurement by connecting the working electrode to the activation contact (ITO|Au|ITO) in a three-electrode configuration in the electrolyte with ambient light. A typical series of CV scans for varying activation cycles is shown in Figure s5. CV scans at a fast scan rate (100 mV/s) were able to activate the NiO_x-TX OER catalyst within the first 40 cycles for 7 minutes. Positions of the oxidation peak initially dropped and then shifted to slightly higher potential (0.63 V, red curve in Figure 3e) indicating an inherent and enhanced β/β transition. This observation is consistent with the experiments conducted on FTO glasses. However, no significant shift in the reduction peak position (black curve in Figure s5) was noticed and thus an enlarged difference between oxidation and reduction peaks with the increasing activation cycles. This observation suggested a

poor reversibility with the activation cycles. One can also see an increase of the magnitude of the oxidation peaks from 0.27 to 4.28 mA/cm^2 with the varying activation cycles and a saturation appearing after 40 cycles of scan (red curve in Figure s5). Although the reduction peak magnitude also increased with the activation cycles, the difference over the oxidation peak magnitude indicates an incomplete reduction which could lead to a degradation of performance and loss of efficiency[48]. Most importantly, OER current densities at the overpotential of 493 mV first dropped during the first 3 cycles of scan and then immediately shot up and saturated after 40 cycles of scan (red curve in Figure s5). Also, the overpotential to reach 1 mA/cm^2 OER current density in the oxidation branch increased initially and eventually dropped by 75 mV after 40 activation cycles (black curve in Figure s5). Therefore, the activation of the NiO$_x$-TX OER catalyst within the potential window for 40 cycles was really effective to improve the catalytic activity. The water oxidation current density at the overpotential of 493 mV increased about 4 times from 3.2 to 12.1 mA/cm^2.

The PEC performance of the activated electrodes was then measured by switching the working electrode from the activation contact on the ITO|Au|ITO to the back contact of the Si (Experimental session). CV scans under illumination and in the dark are shown in Figure 4b. The reduced onset potential and the overpotential needed to drive a certain current density compared to the one measured directly through the activation contact (dark cyan curve in Figure 4b) were due to the photo voltage generated from the ITO|n-Si Schottky junction (magenta curve in Figure 4b) and the np$^+$-Si junction (black curve in Figure 4b). The onset potential was reduced by 270 mV and 380 mV on ITO|n-Si Schottky junction and np$^+$-Si junction, respectively. Current saturation was observed within a low bias (< 500 mV) for the np$^+$-Si junction based photoanode. Tafel slope at the current density of 1 mA/cm^2 on ITO|Au|ITO|NiO$_x$-TX is 63.2 mV/dec, n-

Si|ITO|Au|ITO|NiO$_x$-TX is 203.9 mV/dec, and np$^+$-Si|ITO|Au|ITO|NiO$_x$-TX is 97.4 mV/dec (Figure 4c).

The mechanism we proposed is illustrated in Figure 4d using the energy band diagrams based on the actual measurement results shown in Figure 4b. To maintain a current density of 1 mA/cm^2 on the ITO|Au|ITO|NiO$_x$-TX, an overpotential of at least 350 mV was required which includes the activation overpotential and uncompensated resistance loss. Note that the OER reaction potential at pH=13.8 from calculation is located at 0.415 V. This results in an external bias of 0.76 V required to drive this amount of the OER current density. When n-Si was added to the backside of ITO, the V$_{oc}$ (~270 mV) upon illumination shifted the external bias that is needed to reach 1 mA/cm^2 cathodically by 220 mV. On the other hand, when an np$^+$-Si junction was added to the ITO, this structure was able to further shift the onset potential cathodically, as well as the bias needed to drive the OER current density by 380 mV under illumination. This resulted in a reduced external potential required to drive the OER current. Higher Tafel slopes on the Si photoanodes were believed due to the series resistance loss across the Si junction as well as the Si ITO interface (contact resistance and substrate resistance). This also can be noticed from the finite slope of I-V curves cross the x-axis in Fig. 4a. To further achieve a photocurrent of 8.13 mA/cm^2, an overpotential of 450 mV and 200 mV were needed on the catalyst and the np$^+$-Si photoanode, respectively.

To enhance the hole-conduction to the traditional n-TCO, we developed a sandwich TCO where a thin Au layer was sandwiched in between ITO. The average transmittance of the sandwich TCO in the wavelength range of 360-1100 nm was about 70% after the same annealing process as the NiO$_x$-TX precursor, which is comparable to the as-deposited bare ITO (78%) (Fig. s6). Annealing improved the transmittance of the ITO, but degraded its conductivity. However,

the sandwich TCO was able to reach a low resistivity (0.43 mΩ•cm) after annealing, 6 times

smaller than that for the annealed bare ITO (2.4 mΩ•cm). Most importantly, the bare ITO coated

n-Si showed significant degradation during the measurement which has been reported

previously[25]. The electrochemical stability of ITO is strongly environment and bias dependent.

ITO is not stable in reductive or acidic environment due to its tendency to be reduced to metallic

phase (tin metal). However, ITO is much more stable in base under anodic conditions.

Experiments have been conducted and showed that the stability of ITO greatly depends on the

oxygen partial pressure, deposition power, substrate heating, and current density, which in-turn

strongly affect the defects and oxygen vacancies on the ITO stability. To stabilize the ITO, it was

suggested that using a thin layer of noble metal nanoparticles such as Au on the surface. Due to

the strong faradaic interference, we did not want Au in direct contact to the electrolyte, because

Au could cause strong interference to the OER reaction on the NiO_x. On the other hand, we did

not strongly mix the Au and ITO through co-sputtering or directly deposit Au on Si substrate

which can diffuse further into Si buried junction and/or cause potential delamination because of

the poor adhesion without an adhesion layer. Although the Au is sandwiched between ITO films,

it can still carry majority applied current, as one can see in later discussions. Most importantly,

the low work function ITO (~4.7 eV) can be tuned by changing the Stoichiometry or surface

chemistry. Utilization of a high work function noble metal can be used to increase the work

function of ITO for hole injection in light emitting diode[49] and hole extraction in solar cell[50], in

which the high work function metal could effectively lower the hole transport barrier.

Furthermore, the Au interlayer reduced not only the series resistance of the ITO film, but also the

contact resistance to the p^+-Si due to the increased work function and thus reduced barrier height

for holes. In addition, ITO|Au|ITO could deplete the NiO_x which could minimize the unfavorable

surface band bending at the p-type NiO$_x$ electrolyte interface for a facilitated charge transfer and minimized light response. The effect of the intermediate Au and the resulting high work function on the electronic and catalytic properties of NiO$_x$ is unknown. Therefore, the extended work could be focused on developing fundamental understanding on the hole transport properties of this sandwich TCO, as well as the interfacial energetics including the work function.
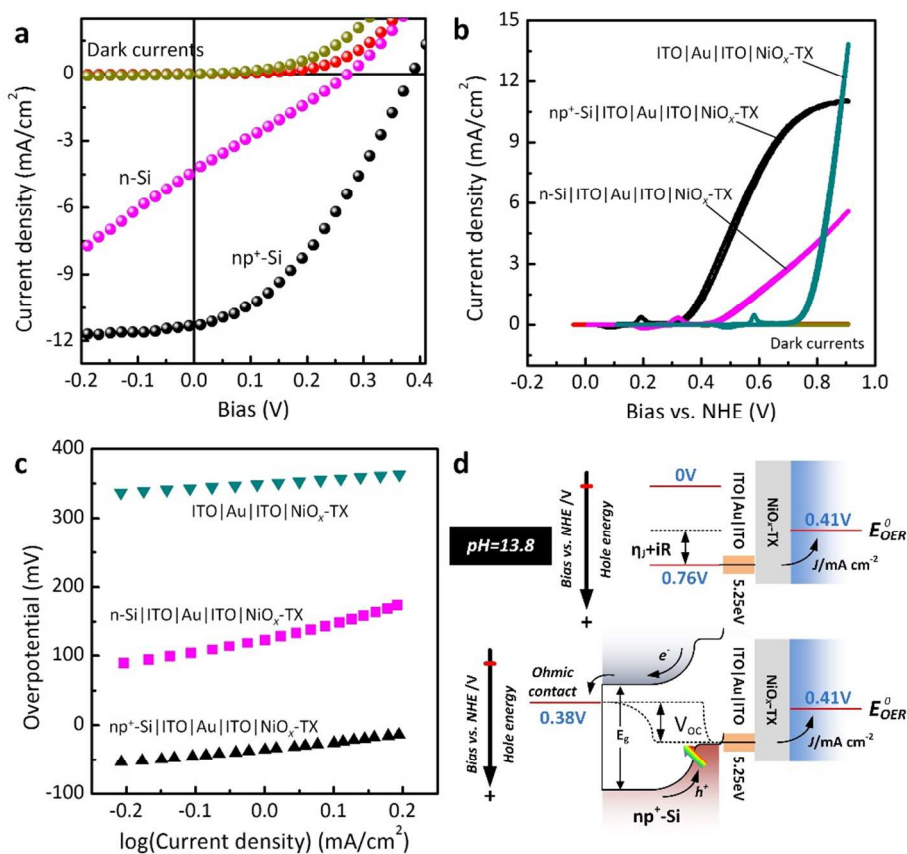
Fig.4 (a) Comparison of the photovoltaic performances of the n-Si|ITO|Au|ITO Schottky junction and the Si np$^+$-junction solar cell measured under attenuated light. (b) CV curves and (c) Tafel slopes of the photoanodes across the water oxidation current density of 1 mA/cm^2. (d) Energy band diagrams of the NiO$_x$-TX OER catalyst on a conducting substrate (top) and on np$^+$-Si junction photoanode (bottom). Energy band diagram for n-Si is not shown.

np^+-Si|ITO|Au|ITO|NiO$_x$-TX photoanode: We have performed detailed studies on the np^+-Si based photoanode with regarding the incident light intensity, stability and pH effects. Light intensity effect on the solar cell performance was studied by applying a series of neutral density (ND) filters with the sample in the measurement setup where light was attenuated. Samples were also measured in air with unmasked solar simulated light intensity of 1 sun at the sample position (100 mW/cm^2, navy blue curve in Figure 5a). Under this standard condition, a V_{oc} of 424 mV, a J_{sc} of -22.43 mA/cm^2, a light-limited current density of -24.51 mA/cm^2, a fill factor (FF) of 30.79% and a conversion efficiency of 2.93% were achieved using the np^+-Si photovoltaic cell. While under attenuated light in the PEC measurement setup where intensity was measured 51.2 mW/cm^2, a V_{oc} of 388 mV, a J_{sc} of -11.30 mA/cm^2, a FF of 36.97% and a conversion efficiency of 3.17% were achieved (black curve in Figure 5a). It was observed that V_{oc} increased linearly, while J_{sc} increased linearly with the increasing light intensity (Figure 5b). The inferior photovoltaic behavior can be contributed by several non-optimized fabrication conditions, including the doping concentrations and the junction depth. For example, a high doping in the emitter results in a high recombination, although reduces the resistance loss. Meanwhile, oxide residuals on the surface may result in a high resistance loss and a high thermal shot (RTA) results in the crystal damage, which increases the density of recombination centers. Extended work is currently conducted in the group including using Si HIT (Heterojunction with Intrinsic Thin-layer) cell with a high V_{oc}, which will be reported elsewhere.

PEC performance was also measured under different light intensities and displayed in Figure 5c. Saturation of the photocurrent at a low overpotential was noticed due to the light limited carrier generation. The solar to oxygen conversion efficiency (SOCE) under 0.51-sun illumination can be calculated by

$$SOCE = \frac{|V_{onset} - E^0| \cdot J_{H_2O/O_2} \cdot FF}{I_{ph}}$$

where V_{onset} is the overpotential when water oxidation current starts typically after the Ni oxidation peak, E^0 is the equilibrium water oxidation potential at 1 M NaOH solution, which is calculated of 0.415 V, and $J_{H2O/O2}$ is the current density at the E^0. The data used for this efficiency calculation was based on a three-electrode configuration. Therefore only the half reaction on the photoanode was considered. The calculated SOCE, representing the upper limit of the conversion efficiency under applied bias[51], is 0.07% (inset Figure 5c).

A smaller V_{oc} caused by the reduced light intensity effectively shifted the Ni reduction/oxidation peaks and the onset water oxidation potential to higher anodic potentials approaching to the position directly measured through the activation contact. The magnitudes of the peaks were effectively reduced (Figure s7) and the shapes of the peaks were broadened with the decreasing light intensity. Similar to light intensity dependent J_{sc} (blue curve in Figure 5b), the saturation current density measured at 0.908 V decreased linearly with the decreasing light intensity (Figure 5d). Linear relationship between the J_{sc} and the light intensity indicated that the charge generation and transportation in the np^+-Si junction was the rate-limiting step. Therefore, the catalytic reaction at the NiO_x catalysts as well as the mass transfer in the electrolyte was very efficient, which did not limit the water oxidation process at the corresponding current levels.
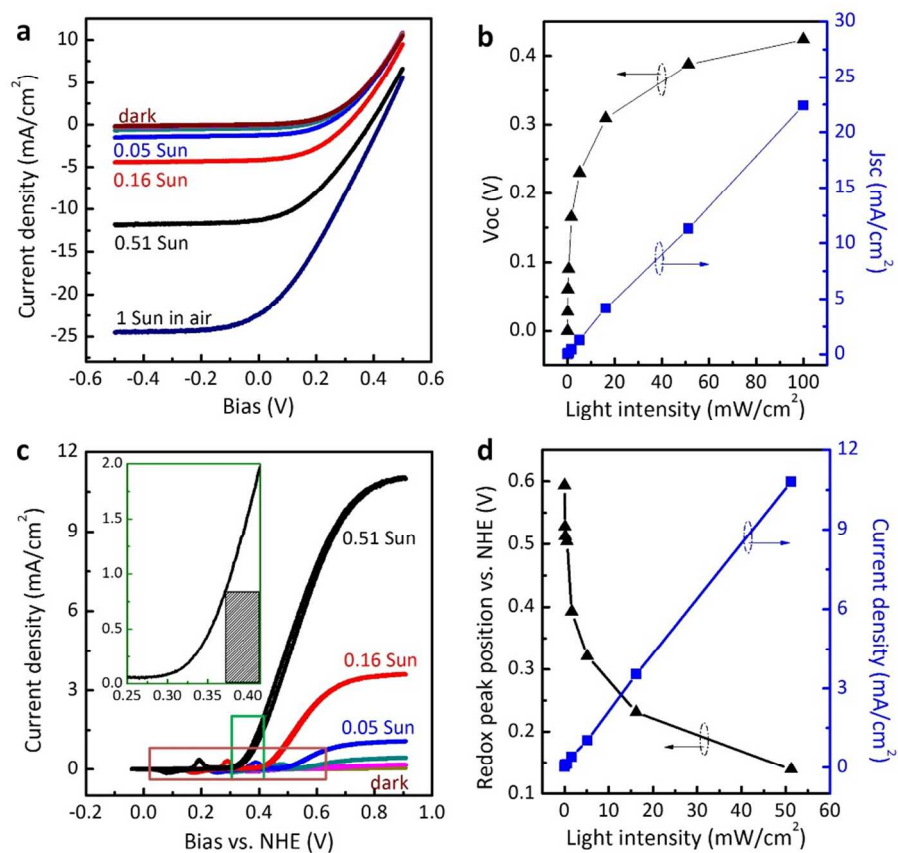
Fig.5 (a) I-V curves of the np[+]-Si solar cell under different light intensities measured in the PEC measurement setup and in air. (b) V_{oc} and J_{sc} vs. light intensity. (c) CV curves of the np[+]-Si|ITO|Au|ITO|NiO$_x$-TX photoanode under different light intensities. (d) Saturation current density at 0.908 V vs. NHE and redox position of Ni vs. light intensity.

The chemical stability and lifetime of the np[+]-Si|ITO|Au|ITO|NiO$_x$-TX photoanode was studied in an oxidative environment. Figure 6a shows the comparison of CV scans (10 mV/s) taken before and after 360 cycles of the CV studies with a scan rate of 100 mV/s under 0.51-sun illumination. Note that the current density were normalized to show the degradation after 360 scans. Ni reduction/oxidation peaks showed anodic shift while the current density was reduced within the bias window. No saturation was noticed at the overpotential of 493 mV after 360

cycles. Analysis showed that the Tafel slope increased from 97.4 mV/dec to 105.2 mV/dec and

the current density dropped 5% at the overpotential of 493 mV. However, the solid-state

photovoltaic I-V analysis under illumination revealed that no degradation occurred on the Si np$^+$-

junction photovoltaic unit after all the PEC measurement (red and blue curves in Figure 6b). This

also suggested that no significant conductivity change was observed in the s-TCO film[25],

indicating a well-protected Si substrate by the s-TCO in extreme alkaline conditions with an

addition of Au intermediate layer[52]. Therefore, the performance degradation of the photoanode

(Figure 6a) may be caused by a deterioration at the ITO|NiO$_x$-TX interface due to the potential

delamination) and/or a decomposition of the NiO$_x$-TX OER catalyst (Figure s8).
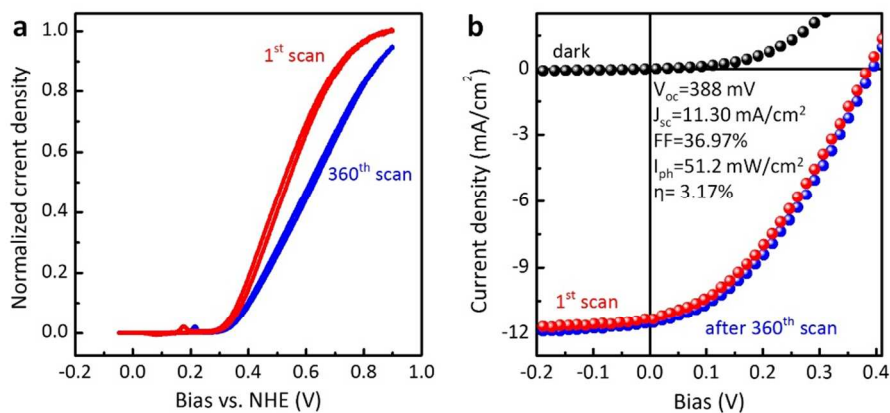
Fig.6 (a) Degradation of the photoanode after 310 cycles of scans under 0.51 sun illumination.
(b) Stable performance of the np$^+$-Si solar cell.

Resistive (iR) losses from p$^+$-Si substrate and ITO|Au|ITO are negligible based on the

geometry and resistivity. The small potential drop in these two layers facilitates the hole

transportation to the catalysts, which thus suppresses the recombination, increases the

photocurrent and the fill factor. However, iR fitting on the CV curves measured after activation

of the OER catalyst showed about an 8-9 ohm loss in the p$^+$-Si|ITO|Au|ITO|NiO$_x$-TX electrode

(black curve) compared to ITO|Au|ITO|NiO$_x$-TX electrode (red curve in Figure 7a). This number

suggested that an additional loss mechanism was involved in the electrode since no changes were

made to the cell configuration during the switching of contact and thus no changes to the

uncompensated solution resistance loss. This additional loss was recognized from the substrate

including effects from the native oxide between ITO and Si, and between GaIn eutectic liquid

metal (ELM) and Si, as well as the contact resistance loss between the ITO and Si.

The as-prepared photoelectrodes were also measured in a neutral pH environment made of

PBS buffered Na$_2$SO$_4$ electrolyte (pH=7.2). The catalyst activation was also conducted in this

neutral electrolyte. Different from the activation behavior typically noticed in a NaOH solution

(Figure s5), the activation CV scans in a neutral pH did not show an improved catalytic activity.

The CV curves of the n-Si|ITO|Au|ITO|NiO$_x$-TX photoanodes, as an example, after activation in

a different environment are shown in Figure 7b. Both electrodes showed a significant increase in

the current density after the water oxidation potential. No Ni reduction/oxidation peaks were

noticed on the electrode measured in the neutral pH environment. Overpotential needed for a

current density of 1 mA/cm^2 for water oxidation is much larger (417 mV) than the sample

measured in the NaOH electrolyte (127 mV). This is presumably due to the lower activity of the

alkaline metal oxide catalyst in a neutral electrolyte, a lower concentration of available OH$^-$ ions

that results in a higher activation barrier, and a potentially poisoning of the catalyst in PBS

buffered electrolyte.
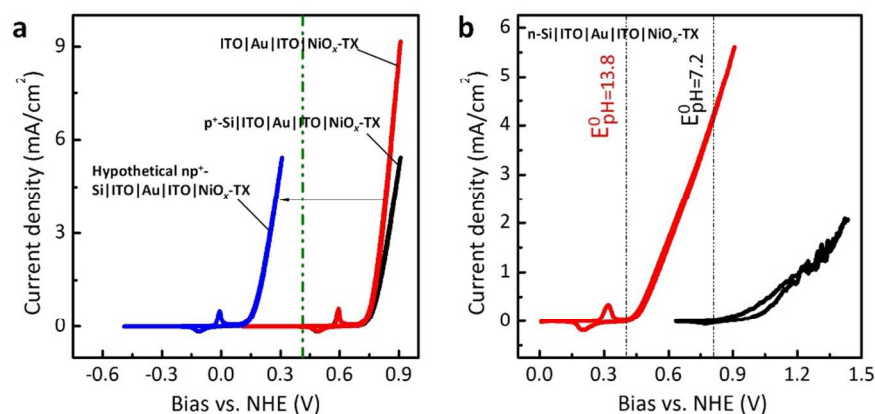
Fig.7 (a) CV curves showing additional ohmic losses. Red curve measured through the ITO|Au|ITO activation contact and black curve measured through the back contact of p^+-Si on p^+-Si|ITO|Au|ITO|NiO$_x$-TX photoelectrode. (b) CV curves showing the pH effect on the photoanodic performance.

Discussions:

Note that among the four elements in the first row transition metals (Mn, Fe, Co and Ni) which hold great promises to replace the noble metal based OER catalysts for a large-scale solar fuel conversion, a Ni based OER catalyst is believed to outperform others based on the theoretical and experimental studies[53, 54]. The activity of the NiO$_x$ OER catalyst prepared from the solution-casted precursors depends greatly on the annealing process. Overheating the precursors even at a considerably low temperature with the hope of improving crystallinity can degrade its catalytic activity. The β-Ni(OH)$_2$/β-NiOOH transition is recognized as a more active phase transition in the NiO OER catalyst. The activation process is typically used on amorphous catalysts either from a constant or a cycling current/bias[55-57]. The conditioning of catalysts using a constant

anodic current on a Ni-B$_i$ OER catalyst can also induce a change of structure and valence state of Ni[56]. This conditioning on the catalyst enhanced the activity greatly depends on the concentration of the conditioning solution. Yeo and Bell prepared β-Ni(OH)$_2$ by cycling the Ni metal electrode from the α-Ni(OH)$_2$ in concentrated KOH for up to 15 hrs[57]. The β-Ni(OH)$_2$ from their experiment also showed the anodically shifted reduction/oxidation peaks. Activation process is also applied to other catalysts[58]. The addition of foreign molecules by forming metal-surfactant complexes and the control over the thermal treatment process can effectively lower the energy input needed to achieve an intrinsically activate catalyst. Amorphous electrocatalyst without activation process are desired through an introduction of doping[59] or carbon-composites[60]. Alternatively, a mesoporous structure can be also applied[61, 62]. This can be realized by impregnation and calcinations of precursors on a mesoporous template and subsequent removal of the template, providing enhanced surface reaction sites and a potential photon trapping.

Also note that utilizing a hypothetical crystal Si single junction substrate with a 600-mV V$_{oc}$, 30-mA/cm^2 J$_{sc}$, and stabilized by a TCO coating with a minimum light loss, one can further cathodically shift the onset potential, e.g., Si HIT cell[63]. A minimum 10 mA/cm^2 photocurrent at the E$_{OER}$ can be achieved based on a rough estimation on the blue curve in Figure 4h. However, the maximum SOCE is limited by the single junction Si solar cell due to the large overpotential needed to drive an efficient water oxidation current using the earth abundant transition metal based catalysts, which typically need ~400 mV to drive a 8.13-mA/cm^2 OER current[64]. This results in a SOCE above 0.4% using the ultrathin NiO$_x$ OER catalyst on a hypothetical cell, suggesting a further development of the hole conducting TCO and better Si pn junction are important.

30

One figure-of-merit to evaluate the photoelectrode performance is the current density at the water oxidation equilibrium potential (E_0) in different electrolytes, and the other is the Tafel slope. However, the Tafel slopes reported in respective literatures are measured at different current densities, and direct comparison of the reported numbers does not lead to consistency. To be fair, we have extracted the reported data and calculated the Tafel slopes at the current density of 1 mA/cm^2. Comparative performances of the Si based photoanodes for water oxidation from previous reported work are summarized in table 1. The device presented in this work shows comparable a current density at the water oxidation potential to others despite it being measured under 0.51-sun intensity. Prediction based on the solid-state device performance under 1-sun condition shows that the as-reported photoanode is capable to provide a photocurrent of ~5 mA/cm^2 at E_0 and a current density of ~22 mA/cm^2 at the overpotential of 493 mV.

Annealing temperature and time are important factors, which needs to be controlled to reach an optimized activity of a catalyst by decomposing a solution phase precursor[59]. Besides, the ratio between the complexing agent and the nickel salt is the other parameters affecting the activity. It was noticed in this study that the activity of the NiO$_x$-TX catalyst reached a local maximum after annealing for a shorter time[35]. Moreover, this catalyst showed an anodic shift of the redox peak position during the cyclic activation process. A systematic study including using surfactant with a smaller molecular size, varying the concentration of the surfactant, the anion effect in the nickel precursor, introducing doping with other transition metals[65], controlling the annealing temperature and environment, and their effects on the NiO$_x$ activity and stability are current conducted in our lab. In this work, Au was used in the ITO to tune its electrical properties in this work for demonstration. It will be interesting to examine the earth abundant transition metals with a high work function (such as Cu, Ni, Mo, and etc) and the possibilities to replace the Au in

the ITO as a window layer for hole transportion[52, 53]. It will be also interesting to develop transition metal based p-type TCO to further replace the use of indium. In terms of the diffusion of solar cell fabrication, the dimension and doping concentration of the surface inverted layer needs to be optimized to minimize the light absorbed in the p-layer and maximize the junction depth for an efficient charge generation in the n-Si. Albeit no significant degradation in performance observed, the long-term stability under constant bias needs to be addressed and improved by controlling the precursor composition and annealing/activation conditions.

Table.1 Comparative performance of Si based photoanode structures with various catalysts.

Structure	$J/\ \mathrm{mA \cdot cm^{-2}}$ @ E_{OER}	$b/\ \mathrm{mV\ dec^{-1}}$ @ $J=1\ \mathrm{mA\ cm^{-2}}$	Condition	Reference
n-Si|α-Fe$_2$O$_3$	1.86	132.2	100mW cm^{-2} 1 M NaOH (aq)	21
n-Si|SiO$_x$|TiO$_2$|Ir	8.34	107.5	100mW cm^{-2} 1 M NaOH (aq)	8
n-Si|MnO	5.3	-	100mW cm^{-2} 1 M KOH (aq)	24
n-Si|SiO$_x$|NiO$_x$	0.13	461	100mW cm^{-2} 0.25 M PBS Na$_2$SO$_4$ (aq)	23
npp$^+$-Si|ITO|CoP$_i$	0.86	307.9	100mW cm^{-2} 0.1 M K-P$_i$ (aq)	25

npp$^+$-Si|FTO|NiB$_i$	3.81	72.5	100mW cm^{-2} 0.5 M K-B$_i$ 1.5 M KNO$_3$ (aq)	[26]
npp$^+$-Si|FTO|NiFeO	1.9	119		
n-Si|SiO$_x$|Ni	10.47	64.23	200mW cm^{-2} 1 M NaOH (aq)	[20]
np$^+$-Si|ITO|Au|ITO|NiO$_x$-TX	1.97	97.4	51mW cm^{-2} 1 M NaOH (aq)	This work

Conclusions:

Metal oxides nanoparticles from a sol-gel method can be a promising candidate OER catalyst to photoanodes due to its facile synthesis and high activity. The Au sandwiched in ITO have demonstrated to stabilize the instable Si, efficient hole conduction, and reduce the contact and film resistance. Much higher energy conversion efficiency can be expected by using an optimized Si solar cell with higher photovoltage and long wavelength response for device integration purpose. The developed ultrathin OER catalyst, along with the stable semi-transparent ITO\|Au\|ITO protection layer, is broadly applicable to other photoanode structures, such as III-V compound semiconductor solar cells, which normally need to be stabilized and have much higher efficiency.

Competing financial interests:

The authors declare no competing financial interests.

Additional information: Stability of the NiO_x-TX catalyst; XPS and XANES spectrum of samples prepared with different TX concentration and NiOx-TX annealed for different amount of time; p^+-Si|NiO_x electrode, ITO, FTO and ITO|Au|ITO electrode; light loss evaluation through measurement setup and water absorption; in-situ catalyst activation process; transmittance and resistivity of ITO films with and without intermediate Au before and after annealing on a hotplate; redox potential position vs. light intensity on a buried junction photoanode; degradation of NiO_x-TX catalyst after 200 cycles of scans.

References:

1.   H. B. Gray, *Nat. Chem.*, 2009, **1**, 7-7.

2.   N. S. Lewis and D. G. Nocera, *Proc. Natl. Acad. Sci. USA*, 2006, **103**, 15729-15735.
3.   S. Chen and L.-W. Wang, *Chem. Mater.*, 2012, **24**, 3659-3666.
4.   M. G. Walter, E. L. Warren, J. R. McKone, S. W. Boettcher, Q. Mi, E. A. Santori and N. S. Lewis, *Chem. Rev.*, 2010, **110**, 6446-6473.
5.   F. R. F. Fan, G. A. Hope and A. J. Bard, *J. Electrochem. Soc.*, 1982, **129**, 1647-1649.
6.   P. A. Kohl, S. N. Frank and A. J. Bard, *J. Electrochem. Soc.*, 1977, **124**, 225-229.
7.   H. Tsubomura, Y. Nakato, M. Hiramoto and H. Yano, *Can. J. Chem.*, 1985, **63**, 1759-1762.
8.   Y. W. Chen, J. D. Prange, S. Dühnen, Y. Park, M. Gunji, C. E. D. Chidsey and P. C. McIntyre, *Nat. Mater.*, 2011, **10**, 539-544.
9.   J. Qiu, P. Pavaskar, G. Zeng, Z. Li and S. B. Cronin, *PCCP*, 2013.
10.   K. Sun, K. Madsen, P. Andersen, W. Bao, Z. Sun and D. Wang, *Nanotechnol.*, 2012, **23**, 194013.
11.   R. H. Coridan, M. Shaner, C. Wiggenhorn, B. S. Brunschwig and N. S. Lewis, *J. Phys. Chem. C*, 2013, **117**, 6949-6957.
12.   K. Fujii, T. Kato, K. Sato, I. Im, J. Chang and T. Yao, *Phys. Status Solidi C*, 2010, **7**, 2218-2220.
13.   H. Morisaki, H. Ono, H. Dohkoshi and K. Yazawa, *Jpn. J. Appl. Phys.*, 1980, **19**, L148.
14.   L. Thompson, J. DuBow and K. Rajeshwar, *J. Electrochem. Soc.*, 1982, **129**, 1934-1935.
15.   G. Hodes, L. Thompson, J. DuBow and K. Rajeshwar, *J. Am. Chem. Soc.*, 1983, **105**, 324-330.
16.   D. Bélanger, J. P. Dodelet and B. A. Lombos, *J. Electrochem. Soc.*, 1986, **133**, 1113-1119.
17.   H. Cachet, J. Bruneaux, G. Folcher, C. Lévy-Clément, C. Vard and M. Neumann-Spallart, *Sol. Energy Mater. Sol. Cells*, 1997, **46**, 101-114.
18.   F. Decker, M. Fracastoro‐Decker, W. Badawy, K. Doblhofer and H. Gerischer, *J. Electrochem. Soc.*, 1983, **130**, 2173-2179.
19.   W. A. Badawy, *Sol. Energy Mater. Sol. Cells*, 2002, **71**, 281-294.
20.   M. J. Kenney, M. Gong, Y. Li, J. Z. Wu, J. Feng, M. Lanza and H. Dai, *Science*, 2013, **342**, 836-840.
21.   K. Jun, Y. S. Lee, T. Buonassisi and J. M. Jacobson, *Angew. Chem. Int. Ed.*, 2012, **51**, 423-427.
22.   K. Sun, X. Pang, S. Shen, X. Qian, J. S. Cheung and D. Wang, *Nano Lett.*, 2013, **5**, 2064-2072.
23.   K. Sun, N. Park, Z. Sun, J. Zhou, J. Wang, X. Pang, S. Shen, S. Y. Noh, Y. Jing, S. Jin, P. Yu and D. Wang, *Energy Environ. Sci.*, 2012, **5**, 7872-7877.
24.   N. C. Strandwitz, D. J. Comstock, R. L. Grimm, A. C. Nichols-Nielander, J. Elam and N. S. Lewis, *J. Phys. Chem. C*, 2013, **117**, 4931-4936.
25.   J. J. H. Pijpers, M. T. Winkler, Y. Surendranath, T. Buonassisi and D. G. Nocera, *Proc. Natl. Acad. Sci. USA*, 2011, **108**, 10056-10061.
26.   C. R. Cox, M. T. Winkler, J. J. H. Pijpers, T. Buonassisi and D. G. Nocera, *Energy Environ. Sci.*, 2012, **6**, 532-538.
27.   S. Mubeen, J. Lee, N. Singh, M. Moskovits and E. W. McFarland, *Energy Environ. Sci.*, 2013, **6**, 1633-1639.
28.   R. Noufi, A. J. Nozik, J. White and L. F. Warren, *J. Electrochem. Soc.*, 1982, **129**, 2261-2265.
29.   R. A. Simon and M. S. Wrighton, *Appl. Phys. Lett.*, 1984, **44**, 930-932.
30.   T. Skotheim, L. G. Petersson, O. Inganas and I. Lundstrom, *J. Electrochem. Soc.*, 1982, **129**, 1737-1741.
31.   A. G. Scheuermann, J. D. Prange, M. Gunji, C. E. D. Chidsey and P. C. McIntyre, *Energy Environ. Sci.*, 2013.
32.   N. S. Lewis, *Science*, 2007, **315**, 798-801.
33.   A. C. Nielander, M. J. Bierman, N. Petrone, N. C. Strandwitz, S. Ardo, F. Yang, J. Hone and N. S. Lewis, *J. Am. Chem. Soc.*, 2013.
34.   E. R. Young, R. Costi, S. Paydavosi, D. G. Nocera and V. Bulovic, *Energy Environ. Sci.*, 2011, **4**, 2058-2061.

35.   L. Trotochaud, J. K. Ranney, K. N. Williams and S. W. Boettcher, *J. Am. Chem. Soc.*, 2012, **134**, 17253-17261.

36.   M. E. G. Lyons and M. P. Brandon, *Int. J. Electrochem. Sci.*, 2008, **3**, 1386-1424.

37.   H. Bode, K. Dehmelt and J. Witte, *Electrochim. Acta*, 1966, **11**, 1079-1087.

38.   G. M. Canfield, M. Bizimis and S. E. Latturner, *Chem. Mater.*, 2009, **22**, 330-337.

39.   P. Matejka, B. Vlckova, J. Vohlidal, P. Pancoska and V. Baumruk, *J. Phys. Chem.*, 1992, **96**, 1361-1366.

40.   E. Stathatos, P. Lianos and C. Tsakiroglou, *Microporous Mesoporous Mater.*, 2004, **75**, 255-260.

41.   in *Metal Oxide Nanoparticles in Organic Solvents*, Springer London, 2009, ch. 2, pp. 7-18.

42.   I. T. Kim, G. A. Nunnery, K. Jacob, J. Schwartz, X. Liu and R. Tannenbaum, *J. Phys. Chem. C*, 2010, **114**, 6944-6951.

43.   J. C. De Jesus, I. González, A. Quevedo and T. Puerta, *J. Mol. Catal. A: Chem.*, 2005, **228**, 283-291.

44.   L. Znaidi, G. J. A. A. Soler Illia, S. Benyahia, C. Sanchez and A. V. Kanaev, *Thin Solid Films*, 2003, **428**, 257-262.

45.   H. Wang, P. Ge, C. G. Riordan, S. Brooker, C. G. Woomer, T. Collins, C. A. Melendres, O. Graudejus, N. Bartlett and S. P. Cramer, *J. Phys. Chem. B*, 1998, **102**, 8343-8346.

46.   K. Sakaino, Y. Kawabata and S. Adachiz, *J. Electrochem. Soc.*, 2000, **147**, 1530-1534.

47.   L. Trotochaud, T. J. Mills and S. W. Boettcher, *J. Phys. Chem. Lett.*, 2013, **4**, 931-935.

48.   K. Provazi, M. J. Giz, L. H. Dall'Antonia and S. I. Córdoba de Torresi, *J. Power Sources*, 2001, **102**, 224-232.

49.   Y. Shen, D. B. Jacobs, G. G. Malliaras, G. Koley, M. G. Spencer and A. Ioannidis, *Adv. Mater.*, 2001, **13**, 1234-1238.

50.   C.-D. Wang and W. C. H. Choy, *Sol. Energy Mater. Sol. Cells*, 2011, **95**, 904-908.

51.   Z. Chen, T. F. Jaramillo, T. G. Deutsch, A. Kleiman-Shwarsctein, A. J. Forman, N. Gaillard, R. Garland, K. Takanabe, C. Heske, M. Sunkara, E. W. McFarland, K. Domen, E. L. Miller, J. A. Turner and H. N. Dinh, *J. Mater. Res*, 2010, **25**, 3-16.

52.   E. Matveeva, *J. Electrochem. Soc.*, 2005, **152**, H138-H145.

53.   J. O. M. Bockris, *J. Chem. Phys.*, 1956, **24**, 817-827.

54.   R. Subbaraman, D. Tripkovic, K.-C. Chang, D. Strmcnik, A. P. Paulikas, P. Hirunsit, M. Chan, J. Greeley, V. Stamenkovic and N. M. Markovic, *Nat. Mater.*, 2012, **11**, 550-557.

55.   P. W. T. Lu and S. Srinivasan, *J. Electrochem. Soc.*, 1978, **125**, 1416-1422.

56.   D. K. Bediako, B. Lassalle-Kaiser, Y. Surendranath, J. Yano, V. K. Yachandra and D. G. Nocera, *J. Am. Chem. Soc.*, 2012, **134**, 6801-6809.

57.   B. S. Yeo and A. T. Bell, *J. Phys. Chem. C*, 2012, **116**, 8394-8400.

58.   H. Vrubel and X. Hu, *Angew. Chem. Int. Ed.*, 2012, **51**, 12703-12706.

59.   R. D. L. Smith, M. S. Prévot, R. D. Fagan, Z. Zhang, P. A. Sedach, M. K. J. Siu, S. Trudel and C. P. Berlinguette, *Science*, 2013, **340**, 60-63.

60.   Y. Liang, Y. Li, H. Wang, J. Zhou, J. Wang, T. Regier and H. Dai, *Nat. Mater.*, 2011, **10**, 780–786.

61.   J. Kibsgaard, Y. Gorlin, Z. Chen and T. F. Jaramillo, *J. Am. Chem. Soc.*, 2012, **134**, 7758-7765.

62.   J. Kibsgaard, Z. Chen, B. N. Reinecke and T. F. Jaramillo, *Nat. Mater.*, 2012, **11**, 963-969.

63.   H.-P. Wang, T.-Y. Lin, C.-W. Hsu, M.-L. Tsai, C.-H. Huang, W.-R. Wei, M.-Y. Huang, Y.-J. Chien, P.-C. Yang, C.-W. Liu, L.-J. Chou and J.-H. He, *ACS Nano*, 2013, **7**, 9325-9335.

64.   A. J. Bard and M. A. Fox, *Acc. Chem. Res.*, 1995, **28**, 141-145.

65.   M. W. Louie and A. T. Bell, *J. Am. Chem. Soc.*, 2013.